

# Selective adsorption of bismuth telluride nanoplatelets through electrostatic attraction†

Cite this: *Phys. Chem. Chem. Phys.*,  
2014, 16, 11297

Lingling Guo,<sup>ab</sup> Amira Aglan,<sup>ab</sup> Haiyu Quan,<sup>ab</sup> Junjie Sun,<sup>bc</sup> Chaolong Tang,<sup>bd</sup>  
Jinhui Song,<sup>bd</sup> Greg Szulczewski<sup>b,e</sup> and Hung-Ta Wang<sup>\*ab</sup>

We demonstrate a facile technique to assemble solution phase-synthesized bismuth telluride ( $\text{Bi}_2\text{Te}_3$ ) nanoplatelets into arrays of micropatterns. Aminosilane self-assembled monolayers (SAMs) are printed on silicon dioxide ( $\text{SiO}_2$ ) substrates using microcontact printing ( $\mu\text{CP}$ ). The SAM printed surfaces are terminated with amine-groups allowing  $\text{Bi}_2\text{Te}_3$  nanoplatelet selective adsorption by electrostatic attraction. Using Kelvin probe force microscopy, the electrical potential difference between aminosilane SAM and  $\text{Bi}_2\text{Te}_3$  nanoplatelet surfaces is found to be  $\sim 650$  mV, which is larger than that ( $\sim 400$  mV) between the  $\text{SiO}_2$  substrate and  $\text{Bi}_2\text{Te}_3$  nanoplatelet surfaces. The selective adsorption provides an opportunity for integrating solution phase-grown topological insulators toward several device-level applications.

Received 16th February 2014,  
Accepted 21st April 2014

DOI: 10.1039/c4cp00690a

www.rsc.org/pccp

## 1. Introduction

The V–VI group chalcogenides, including bismuth telluride ( $\text{Bi}_2\text{Te}_3$ ), bismuth selenide ( $\text{Bi}_2\text{Se}_3$ ), and antimony telluride ( $\text{Sb}_2\text{Te}_3$ ), are three-dimensional topological insulators, whose surfaces are covered by the two-dimensional electron gas (2DEG) from the topological surface states.<sup>1–6</sup> The novel topological surface states are induced by a strong spin–orbit coupling, and the spin carriers are protected against time reversal perturbations, *e.g.*, surface defects and impurities, making the 2DEG spin charge transport essentially dissipation-less.<sup>7</sup> Recent advances in topological insulator research have drawn much attention due to its potential application<sup>8</sup> in the next generation electronics,<sup>9,10</sup> thermoelectrics,<sup>11–14</sup> infrared detectors,<sup>15</sup> and heterogeneous catalysis.<sup>16</sup>

The nontrivial topological surface states of these V–VI group chalcogenides are derived from their unique layered crystal structure. In  $\text{Bi}_2\text{Te}_3$ , five atomic layers in the order of  $\text{Te}_{(1)}\text{–Bi–Te}_{(2)}\text{–Bi–Te}_{(1)}$  form a charge neutral sheet with a thickness of  $\sim 1$  nm, called a quintuple sheet.<sup>17,18</sup> Stacking quintuple sheets along the *c*-axis forms the rhombohedral structure, which is in the  $D_{3d}^5(R\bar{3}m)$  space group.<sup>19,20</sup> The adjacent Bi and Te atomic layers in a quintuple sheet are held by covalent forces; in contrast, the bonding between

neighboring quintuple layers, *i.e.*, between adjacent  $\text{Te}_{(1)}$  atomic layers, is a weak van der Waals interaction.<sup>17,18</sup> Because  $\text{Bi}_2\text{Se}_3$  has a smaller van der Waals gap than  $\text{Bi}_2\text{Te}_3$  and  $\text{Sb}_2\text{Te}_3$ , the spin–orbit coupling in  $\text{Bi}_2\text{Se}_3$  is stronger, and consequently the electronic structures of topological surface states in these V–VI group chalcogenides are also different.<sup>2</sup> Topological surface states in several V–VI group chalcogenides have been revealed by angle-resolved photo-emission spectroscopy,<sup>1,3,4</sup> scanning-tunneling microscopy,<sup>7</sup> and transport measurements.<sup>5,6</sup> Currently, the major challenge hampering the novel 2DEG toward practical applications is that the surface spin charge transport is overwhelmed by the ordinary bulk charges. On the other hand, there is a lack of processing techniques suitable for a large scale, device-level integration.

Previously,  $\text{Bi}_2\text{Te}_3$  and  $\text{Bi}_2\text{Se}_3$  nanoplatelets were synthesized on mica surfaces by a chemical vapor transport (CVT) method.<sup>21</sup> On the atomically-smooth surfaces, the nanoplatelet growth could be controlled precisely along mica's crystal orientation *via* the van der Waals epitaxy. Later, arrays of nanoplatelets as flexible infrared transparent electrodes were also demonstrated.<sup>22</sup> Although the van der Waals epitaxy on mica substrates is suitable for selective growth of chalcogenide-based topological insulators, mica substrates are incompatible with common silicon manufacturing processes, which will limit their use in many applications. In contrast, solvothermal syntheses of  $\text{Bi}_2\text{Te}_3$  nanoplatelets are facile, and nanoplatelets can be transferred to any substrate. As a result, it is important to develop methods for transferring  $\text{Bi}_2\text{Te}_3$  nanoplatelets to well-defined positions on the silicon substrate to advance the potential applications of these topological insulator nanoplatelets.

In this work, we report a practical technique to assemble solution phase-grown  $\text{Bi}_2\text{Te}_3$  nanoplatelets into micropattern arrays by the microcontact printing ( $\mu\text{CP}$ ) technique.<sup>23–25</sup> We demonstrate that  $\text{Bi}_2\text{Te}_3$  nanoplatelets could selectively adsorb

<sup>a</sup> Department of Chemical and Biological Engineering, University of Alabama, Tuscaloosa, AL 35487, USA. E-mail: htwang@eng.ua.edu

<sup>b</sup> Center for Materials for Information Technology (MINT Center), University of Alabama, Tuscaloosa, AL 35487, USA

<sup>c</sup> School of Physics, Shandong University, Jinan, Shandong 250100, China

<sup>d</sup> Department of Metallurgical and Materials Engineering, University of Alabama, Tuscaloosa, AL 35487, USA

<sup>e</sup> Department of Chemistry, University of Alabama, Tuscaloosa, AL 35487, USA

† Electronic supplementary information (ESI) available. See DOI: 10.1039/c4cp00690a



onto the surfaces of aminosilane self-assembled monolayers (SAMs) that were printed on silicon oxide ( $\text{SiO}_2$ ) substrates using  $\mu\text{CP}$ . We used Kelvin probe force microscopy (KPFM) to characterize the surface electrical potentials and measured a  $\sim 650$  mV potential difference between aminosilane SAMs and  $\text{Bi}_2\text{Te}_3$  nanoplatelets. The Coulombic interaction between the protonated amine groups and  $\text{Bi}_2\text{Te}_3$  nanoplatelets enables a robust and scalable method for selectively adsorbing solution phase-grown topological insulator nanoplatelets into micropattern arrays. Such a selective adsorption of topological insulators by aminosilane SAMs also opens the possibilities for topological insulator surface passivation, reduction of ordinary bulk charges, and modification of topological surface states *via* electrostatic gating.<sup>26,27</sup>

## 2. Experimental

Several solvothermal syntheses of  $\text{Bi}_2\text{Te}_3$  nanoplatelets were previously reported using different precursors and growth conditions in a similar reducing environment.<sup>28–32</sup> Our method is based on the approach of Li and co-workers.<sup>28</sup> The  $\text{Bi}_2\text{Te}_3$  nanoplatelets were synthesized using the general autoclave reactor (23 ml) from Parr Instrument Company. Bismuth oxide ( $\text{Bi}_2\text{O}_3$ , 99.9995%), tellurium dioxide ( $\text{TeO}_2$ , 99.9995%), ethylene glycol (EG, Reagent Grade), polyvinylpyrrolidone (PVP, average molecular weight 40 000), and sodium hydroxide flakes (NaOH, 98.7%+) were all purchased from Alfa Aesar. All of the chemicals were used as received without further purification. In a typical synthesis, 0.1865 g of  $\text{TeO}_2$ , 0.1793 g of  $\text{Bi}_2\text{O}_3$ , 0.3044 g of PVP, and 0.3047 g of NaOH were added into 15 ml of EG. The mixture was stirred vigorously at 90 °C for 30 minutes in order to thoroughly dissolve the chemicals in EG. The precursor solution was sealed in the autoclave reactor, and the solvothermal reaction was carried out in the oven at a temperature of 210 °C for 24 hours. The as-grown nanoplatelets were collected by centrifugation, and cleaned by rinsing alternatively in de-ionized (DI) water at room temperature and 1-methyl-2-pyrrolidone (NMP) at 85 °C for five cycles. It was critical to remove PVP thoroughly to obtain clean  $\text{Bi}_2\text{Te}_3$  nanoplatelet surfaces for the selective adsorption. The good solubility of PVP in NMP is likely due to the fact that NMP is the pendant group of the polymer, PVP. At an elevated temperature (85 °C), the solubility of PVP in NMP can be further increased. The cleaned  $\text{Bi}_2\text{Te}_3$  nanoplatelets were characterized by scanning electron microscopy (SEM, JEOL 7000 FE), X-ray diffraction (XRD, Bruker D8 Discover), atomic force microscopy (AFM, Park XE 70), and transmission electron microscopy (TEM, FEI Tecnai F-20).

The elastic poly(dimethylsiloxane) (PDMS) stamps for the  $\mu\text{CP}$  were fabricated by first mixing a Sylgard 184 elastomer and a curing agent (w/w = 10/1) and pouring the mixture over master substrates, which were fabricated by conventional photolithography (Karl Suss MA6) with either the SU8-3025 resist or the Shipley 1818 resist. After baking at 70 °C for 24 hours, the PDMS was peeled off from the master and cut into a  $2 \times 2$  cm stamp. To make the  $\mu\text{CP}$  ink, (3-aminopropyl)trimethoxysilane (APTMS, 97% from Sigma-Aldrich) was diluted in DI water to 1% by volume, sonicated for 3 minutes, and then filtered through a syringe filter (0.2  $\mu\text{m}$

pore size, from VWR). In a standard  $\mu\text{CP}$  process, the PDMS stamp was immersed in the filtered 1% APTMS aqueous solution for 2 minutes and then dried by nitrogen blow. The substrate was an n-type (100) silicon substrate (phosphorus doped, resistivity = 0.001–0.005 ohm cm) with a thermally-grown dry oxide (thickness  $\sim 120$  nm), which was cleaned by rinsing with acetone–IPA, and oxygen plasma treatment before the  $\mu\text{CP}$ . The stamp was brought in contact with the  $\text{SiO}_2/\text{Si}$  substrate for 10–20 s at 50 °C on the hotplate to ensure the transfer of a single molecular layer of APTMS. The APTMS printed substrate was immediately immersed in the  $\text{Bi}_2\text{Te}_3$  nanoplatelet-dispersed aqueous solution for 2–20 minutes under a mild vortex action. Finally, the substrate was rinsed with DI water and blown dry by a nitrogen gun. The nanoplatelet-dispersed aqueous solution used for the adsorption was prepared by diluting 20  $\mu\text{l}$  of highly concentrated, cleaned nanoplatelet solution in 2 ml of DI water, followed by vortex and sonication until a homogeneous nanoplatelet dispersion with a light grey color is obtained. SEM, AFM, and KPFM were used to characterize the APTMS printed and nanoplatelet-adsorbed samples.

## 3. Results and discussion

Fig. 1 presents the structure and chemical characterization of the solution phase-grown  $\text{Bi}_2\text{Te}_3$  nanoplatelets. As shown by SEM (Fig. 1(a and d)), the  $\text{Bi}_2\text{Te}_3$  nanoplatelets have a hexagonal morphology owing to the atomic hexagonal packing in their crystal structure. Interestingly, roughly 50% nanoplatelets have a hole in the center, which may originate from the growth of a heterostructure of  $\text{Bi}_2\text{Te}_3$  nanoplatelets skewered by a Te nanowire as observed in the previous reports.<sup>28,29,32</sup> It is likely that when Te nanowires are dissolved by NaOH,  $\text{Bi}_2\text{Te}_3$  nanoplatelets are detached, leaving a hole in the nanoplatelet center. Quantitative analysis of the EDS spectrum (Fig. 1(b)) yields the atomic composition of Bi and Te to be 39.55% and 60.45%, respectively. The XRD pattern (Fig. 1(c)) of the as-synthesized  $\text{Bi}_2\text{Te}_3$  nanoplatelets can be indexed with the rhombohedral  $\text{Bi}_2\text{Te}_3$  crystal, and is consistent with the standard data file (PDF card no. 15-0863). In Fig. 1(e), high resolution TEM (HRTEM) and selected area electron diffraction (SAED) performed on the  $\text{Bi}_2\text{Te}_3$  nanoplatelet show clear lattice fringes and patterns of hexagonally-symmetric spots, respectively. The AFM topographic image (Fig. 1(f)) indicates that the lateral size of the nanoplatelets is roughly in the range of 500 nm to 3  $\mu\text{m}$ , and the thickness is about 10–100 nm. Collectively, the HRTEM, SAED, and XRD data indicate that our solvothermal synthesis produced highly crystallized  $\text{Bi}_2\text{Te}_3$  nanoplatelets, which is consistent with the report of Li *et al.*<sup>28</sup>

We note that cleaned  $\text{Bi}_2\text{Te}_3$  nanoplatelets have a low affinity for  $\text{SiO}_2$  surfaces using either drop casting or dip coating. A low nanoplatelet coating density was consistently obtained, and it showed trivial dependencies on the nanoplatelet dispersion concentration, transferring (adsorption) time, and  $\text{SiO}_2$  substrate hydrophobic/hydrophilic properties. When a high concentration  $\text{Bi}_2\text{Te}_3$  nanoplatelet dispersion was applied, nanoplatelets tended to aggregate to form clusters in local regions (*i.e.*, nanoplatelets



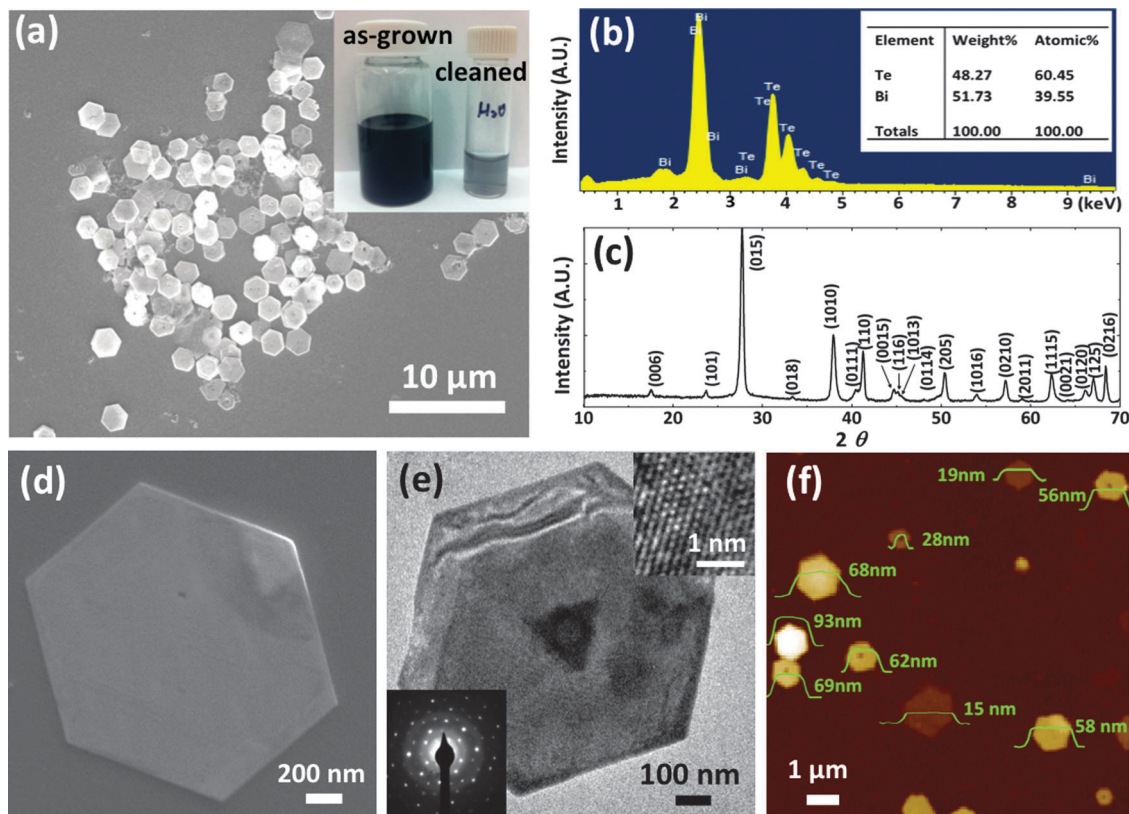


**Fig. 1** (a) SEM image of the cleaned  $\text{Bi}_2\text{Te}_3$  nanoplatelets. Inset: photograph of the vials with as-grown and cleaned nanoplatelet solution. (b) EDS and (c) XRD of cleaned  $\text{Bi}_2\text{Te}_3$  nanoplatelets. (d) High magnification SEM image of the  $\text{Bi}_2\text{Te}_3$  nanoplatelet. (e) TEM image of the  $\text{Bi}_2\text{Te}_3$  nanoplatelet. Insets are HRTEM and SAED, respectively. (f) AFM topographic image of the  $\text{Bi}_2\text{Te}_3$  nanoplatelets with their thicknesses labeled accordingly.

randomly pile up), and most areas were still covered with a low density of nanoplatelets. The low affinity between the  $\text{Bi}_2\text{Te}_3$  nanoplatelets and  $\text{SiO}_2$  surfaces reveals a great challenge in assembling nanoplatelets for practical applications.

To provide a feasible solution, we printed SAMs of APTMS, which were expected to have a strong affinity for the  $\text{Bi}_2\text{Te}_3$  nanoplatelet surface. Fig. 2 demonstrates the selective adsorption of  $\text{Bi}_2\text{Te}_3$  nanoplatelets using the logo of the University of Alabama. The area of the logo "A" consists of an array of APTMS printed houndstooth patterns, and  $\text{Bi}_2\text{Te}_3$  nanoplatelets were adsorbed mainly onto the APTMS printed regions. Interestingly, nanoplatelet aggregation (or stacking) frequently observed before was greatly reduced. More importantly, the selective adsorption can be consistently obtained, and the nanoplatelet coating density could be tuned by varying the adsorption time (shown in the ESI†). This general  $\mu\text{CP}$  of SAMs of aminosilane was first reported for the selective adsorption of negatively-charged nanomaterials by Zhang *et al.*<sup>23</sup> Despite a  $\sim 50\%$  self-catalyzed hydrolysis of (3-aminopropyl)triethoxysilane (APTES) in aqueous solutions at room temperature,<sup>33,34</sup> Zhang *et al.* demonstrated that using hydrophobic PDMS stamps with aqueous APTES inks could still print APTES monolayers. Although the printed APTES did not entirely form SAMs as noted in their work, the amine group terminated surfaces were very effective for the selective adsorption of citrate-coated Au nanoparticles and negatively-charged graphene oxide nanosheets. It is believed that due to

an electrostatic interaction, the negatively-charged nanoparticles/nanosheets are attracted by the positively-charged, protonated amine group surfaces, resulting in a controllable adsorption.<sup>23,35</sup> We demonstrate that this general  $\mu\text{CP}$  technique is very suitable to selectively adsorb topological insulator nanoplatelets.

Although the  $\text{Bi}_2\text{Te}_3$  nanoplatelet selective adsorption could originate from a similar electrostatic interaction, we observed that  $\text{Bi}_2\text{Te}_3$  nanoplatelets had a distinct adsorption behavior than Au nanoparticles.<sup>23,35</sup> By immersing APTMS printed substrates in  $\text{Bi}_2\text{Te}_3$  nanoplatelet dispersed aqueous solutions, a low density of  $\text{Bi}_2\text{Te}_3$  nanoplatelet adsorption with a poor selectivity was obtained surprisingly. In contrast, when a mild vortex was applied during the adsorption of  $\text{Bi}_2\text{Te}_3$  nanoplatelets and while other  $\mu\text{CP}$  conditions were kept the same, the adsorption density was greatly increased and the adsorption selectivity was also improved. Owing to the hexagonally-shaped nanoplatelet morphology, nanoplatelet adsorption onto a planar surface is limited to the top or bottom of nanoplatelet surfaces. When nanoplatelets were dispersed in an unstirred aqueous solution, the nanoplatelets were observed (in an optical microscope) to undergo a flipping-type motion. Owing to the flipping motion, dispersed nanoplatelets had a reduced chance to be in contact with APTMS printed surfaces using the top or bottom nanoplatelet surfaces, and consequently the chance of adsorption reduced. This is different to Au nanoparticle adsorption, as when any point of a sphere surface is in contact with a planar surface, adsorption would easily occur. Upon a mild vortexing-action, the





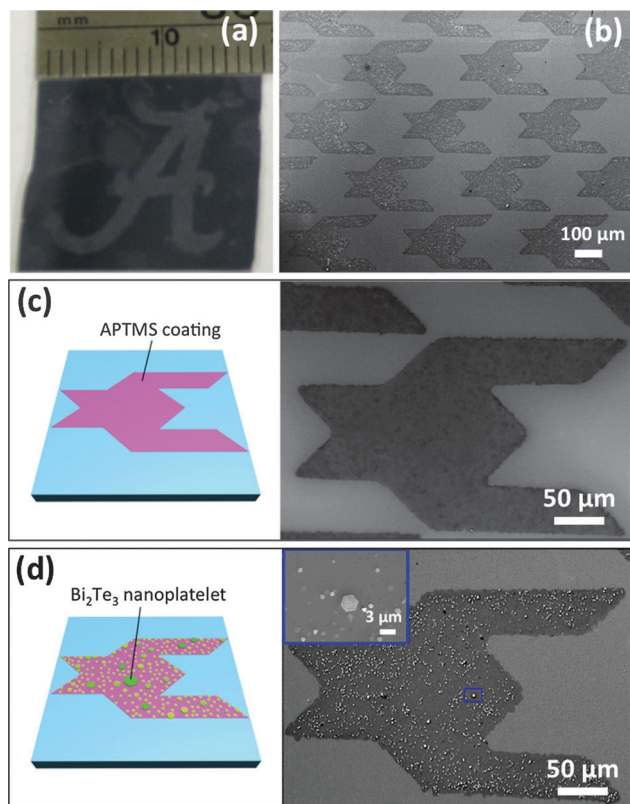


**Fig. 2** (a) Photograph of the silicon chip with selective adsorption of  $\text{Bi}_2\text{Te}_3$  nanoplatelets to reveal logo "A" in which the area consists of a houndstooth array. (b) SEM image of  $\text{Bi}_2\text{Te}_3$  nanoplatelets selective adsorption onto the houndstooth array that is in a local region of logo "A" shown in (a). (c) SEM image of a houndstooth pattern with APTMS coating via  $\mu\text{CP}$ , as illustrated by the cartoon. The dark region is the APTMS coating. (d) SEM image of a houndstooth pattern with the  $\text{Bi}_2\text{Te}_3$  nanoplatelet adsorption, as illustrated by the cartoon. The white dots are nanoplatelets, as magnified in the SEM inset.

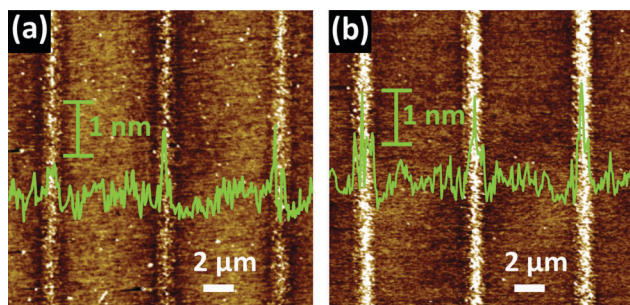


**Fig. 3** AFM topographic images of the APTMS coating prepared by  $\mu\text{CP}$  for 10s (a) without, and (b) with 50 °C *in situ* annealing, respectively. The PDMS stamp contains an array of lines (line width  $\times$  length = 1  $\times$  100  $\mu\text{m}$ ). The topographic profiles (the green lines) are plotted and the scale bar is 1 nm.

$\text{Bi}_2\text{Te}_3$  nanoplatelets in the dispersed aqueous solution constantly collided with the substrate surface, so the chance for a face-to-face contact between nanoplatelet top/bottom surfaces and APTMS surfaces highly increased. At the same time, when nanoplatelets were in contact with bare  $\text{SiO}_2$  surfaces, the low affinity might not be strong enough to retain the adsorption, and nanoplatelets could be carried away by the vortex.

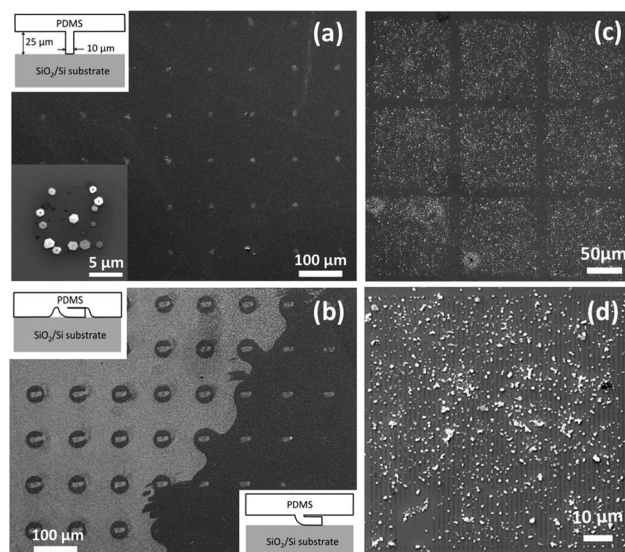


**Fig. 4** (a) SEM image of the selective adsorption of  $\text{Bi}_2\text{Te}_3$  nanoplatelets using an array of 10  $\times$  10  $\mu\text{m}$  squares. The magnified SEM image (inset) shows that the nanoplatelets adsorbed onto the APTMS printed, a 10  $\times$  10  $\mu\text{m}$  square. The square pattern was obtained with the stamp in a normal contact, as illustrated in the inset. (b) SEM image of the selective adsorption of  $\text{Bi}_2\text{Te}_3$  nanoplatelets reveals the two patterns printed with the stamp sagged plus collapsed (left region), and collapsed only (right region), respectively, as illustrated in the insets. Note that these two patterns and the square pattern shown in (a) were obtained from the same substrate. (c) SEM image of the selective adsorption using an array of 1  $\times$  100  $\mu\text{m}$  lines. (d) Magnified SEM image shows that  $\text{Bi}_2\text{Te}_3$  nanoplatelets adsorbed mainly onto the APTMS printed lines.

In order to obtain a stronger electrostatic interaction for  $\text{Bi}_2\text{Te}_3$  nanoplatelet adsorption, we used *in situ* annealing during the  $\mu\text{CP}$  at a temperature of 50 °C. As shown in Fig. 3, the thickness of the APTMS coating clearly increased from 4–20 Å ( $\mu\text{CP}$  at room temperature) to 8–20 Å ( $\mu\text{CP}$  at 50 °C), and the density of APTMS also improved with the *in situ* annealing. It is clear that there are still APTMS particles with a height of  $\sim$ 2 nm formed both with and without an *in situ* annealing, which is likely due to the condensation in the aqueous ink.<sup>23</sup> Excluding those APTMS particles, it is shown that the average APTMS height is 4 Å without *in situ* annealing, and 8 Å with the *in situ* annealing. This implies that APTMS formed sub-monolayers at room temperature, while a better packing was preferred at 50 °C to produce a monolayer.<sup>33</sup> It was previously reported that in toluene (*i.e.*, no hydrolysis effect), *in situ* annealing at 70 °C could improve the packing quality of APTES on  $\text{SiO}_2$  surfaces.<sup>36</sup> This is explained by the fact that the *in situ* annealing facilitates the formation of horizontal Si–O–Si bonds between adjacent APTES molecules, and the effect is an increased packing density. We suspect that the *in situ* annealing during  $\mu\text{CP}$  also improved the APTMS packing quality *via* a similar mechanism (*i.e.*, formation of horizontal Si–O–Si bonds between APTMS). As the amine group density was increased from a closely packed APTMS SAM,  $\text{Bi}_2\text{Te}_3$  nanoplatelet adsorption selectivity was achieved.

We further present the selective adsorption of  $\text{Bi}_2\text{Te}_3$  nanoplatelets using stamps of either a 10  $\times$  10  $\mu\text{m}$  square array



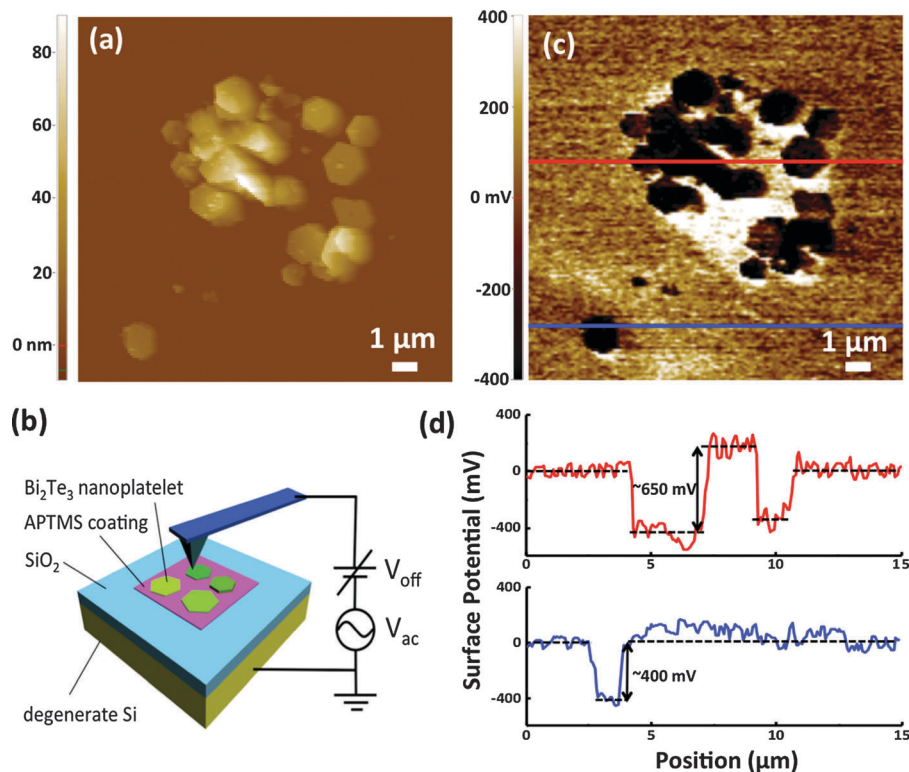


**Fig. 5** (a) AFM topographic image of the Bi<sub>2</sub>Te<sub>3</sub> nanoplatelets adsorbed on the APTMS printed, 10 × 10 μm square region. (b) Schematic of the electrical configuration for the Kelvin probe force microscope measurement. (c) The electrical potential image is scanned in the same area as shown in (a). Note that all nanoplatelets are in the APTMS printed region, except the nanoplatelet in the left/bottom corner that is on the bare SiO<sub>2</sub> surface. (d) The surface electrical potential profiles corresponding to the red and blue line marked in (c) are plotted, respectively.

(as shown in Fig. 4(a and b)) or a 1 × 100 μm line array (as shown in Fig. 4(c and d)). Due to the softness of the PDMS and the dimensions of the square pillar array (shown in Fig. 4(a) inset), the PDMS stamps could sag and/or collapse to cause different μCP patterns.<sup>25</sup> As shown in Fig. 4(a and b), the selective adsorption of Bi<sub>2</sub>Te<sub>3</sub> nanoplatelets reveals the three μCP patterns, induced by the PDMS stamp (1) contacted normally, (2) collapsed plus sagged, and (3) collapsed only, respectively. This result shows that the selective adsorption could be robustly obtained on a 10 × 10 μm APTMS printed surface. To further test the robustness of the selective adsorption, we used PDMS stamps with the 1 × 100 μm line array. Fig. 4(c and d) show that Bi<sub>2</sub>Te<sub>3</sub> nanoplatelets mainly adsorb onto the APTMS printed lines. Indeed, there are still un-wanted nanoplatelets adsorbed on the bare SiO<sub>2</sub> surface due to the affinity between Bi<sub>2</sub>Te<sub>3</sub> nanoplatelets and SiO<sub>2</sub> surfaces. Nevertheless, it should be noted that the line width is comparable with the nanoplatelet lateral size, suggesting that under a vortex motion, the electrostatic interaction between Bi<sub>2</sub>Te<sub>3</sub> nanoplatelets and APTMS printed surfaces is quite reliable to produce the nanoplatelet selective adsorption.

To understand the electrostatic interaction between the APTMS monolayer and the Bi<sub>2</sub>Te<sub>3</sub> nanoplatelet surfaces, we examined the adsorbed Bi<sub>2</sub>Te<sub>3</sub> nanoplatelets by KPFM. As shown in Fig. 5, the surface electrical potential difference between Bi<sub>2</sub>Te<sub>3</sub> surfaces and APTMS printed surfaces is about 650 mV. In comparison, the surface electrical potential difference

between Bi<sub>2</sub>Te<sub>3</sub> surfaces and SiO<sub>2</sub> surfaces is ~400 mV, which is comparable to the report of Hao *et al.*<sup>37</sup> It should be noted that the surface electrical potentials are measured under ambient conditions and not in an aqueous environment. With the existence of electrical double layers formed on the charged surfaces in an aqueous solution,<sup>38</sup> the electrostatic forces experienced by the Bi<sub>2</sub>Te<sub>3</sub> nanoplatelets during the adsorption should be quite different from what was measured by KPFM. Nevertheless, our data implied that in an aqueous solution, the electrostatic attraction force between APTMS surfaces and Bi<sub>2</sub>Te<sub>3</sub> nanoplatelets was stronger than that between bare SiO<sub>2</sub> surfaces and Bi<sub>2</sub>Te<sub>3</sub> nanoplatelets, allowing the selective adsorption of Bi<sub>2</sub>Te<sub>3</sub> nanoplatelets.

## 4. Conclusion

In summary, we have presented a practical method to selectively adsorb solution phase grown topological insulator nanoplatelets onto APTMS printed surfaces *via* μCP. Owing to the specific nanoplatelet morphology, vortex treatment during the adsorption facilitates the nanoplatelet adsorption and simultaneously improves the adsorption selectivity. We also show that APTMS monolayer packing can be improved by *in situ* annealing at 50 °C during μCP, which further enhances the nanoplatelet adsorption. The electrical potential difference, measured by KPFM, between aminosilane SAMs and Bi<sub>2</sub>Te<sub>3</sub> nanoplatelet surfaces is



larger than that between SiO<sub>2</sub> and Bi<sub>2</sub>Te<sub>3</sub> surfaces. We attribute the selective adsorption of Bi<sub>2</sub>Te<sub>3</sub> nanoplatelets to this electrostatic interaction. Such a general adsorption of negatively-charged topological insulators is suitable for a large-scale assembly and device level fabrication.

## Acknowledgements

This work at the University of Alabama (UA) is supported by the UA start-up fund and the 2012 UA Research Grants Committee (RGC) award. L. Guo would like to acknowledge the support from UA MINT Graduate Student Scholarship. A. Aglan would like to acknowledge the support from the National Science Foundation Research Experiences for Undergraduate Program (EEC-1005191; National Academy Grand Challenges), and the UA Emerging Scholar program. J. Sun would like to acknowledge the 2013 Summer Internship Program (SIP) hosted by the UA MINT Center. The authors greatly acknowledge the instrumental support from UA Microfabrication Facility (MFF), UA Central Analytical Facility (CAF), and the UA MINT Center.

## References

- 1 Y. L. Chen, J. G. Analytis, J. H. Chu, Z. K. Liu, S. K. Mo, X. L. Qi, H. J. Zhang, D. H. Lu, X. Dai, Z. Fang, S. C. Zhang, I. R. Fisher, Z. Hussain and Z. X. Shen, *Science*, 2009, **325**, 178–181.
- 2 H. J. Zhang, C. X. Liu, X. L. Qi, X. Dai, Z. Fang and S. C. Zhang, *Nat. Phys.*, 2009, **5**, 438–442.
- 3 D. Hsieh, Y. Xia, D. Qian, L. Wray, J. H. Dil, F. Meier, J. Osterwalder, L. Patthey, J. G. Checkelsky, N. P. Ong, A. V. Fedorov, H. Lin, A. Bansil, D. Grauer, Y. S. Hor, R. J. Cava and M. Z. Hasan, *Nature*, 2009, **460**, 1101–1105.
- 4 Y. Xia, D. Qian, D. Hsieh, L. Wray, A. Pal, H. Lin, A. Bansil, D. Grauer, Y. S. Hor, R. J. Cava and M. Z. Hasan, *Nat. Phys.*, 2009, **5**, 398–402.
- 5 H. L. Peng, K. J. Lai, D. S. Kong, S. Meister, Y. L. Chen, X. L. Qi, S. C. Zhang, Z. X. Shen and Y. Cui, *Nat. Mater.*, 2010, **9**, 225–229.
- 6 D.-X. Qu, Y. S. Hor, J. Xiong, R. J. Cava and N. P. Ong, *Science*, 2010, **329**, 821–824.
- 7 P. Roushan, J. Seo, C. V. Parker, Y. S. Hor, D. Hsieh, D. Qian, A. Richardella, M. Z. Hasan, R. J. Cava and A. Yazdani, *Nature*, 2009, **460**, 1106–1109.
- 8 D. Kong and Y. Cui, *Nat. Chem.*, 2011, **3**, 845–849.
- 9 I. Garate and M. Franz, *Phys. Rev. Lett.*, 2010, **104**, 146802.
- 10 H. Steinberg, D. R. Gardner, Y. S. Lee and P. Jarillo-Herrero, *Nano Lett.*, 2010, **10**, 5036.
- 11 A. Soni, Y. Zhao, L. Yu, M. K. K. Aik, M. S. Dresselhaus and Q. Xiong, *Nano Lett.*, 2012, **12**, 1203–1209.
- 12 R. J. Mehta, Y. Zhang, C. Karthik, B. Singh, R. W. Siegel, T. Borca-Tasciuc and G. Ramanath, *Nat. Mater.*, 2012, **11**, 233–240.
- 13 M. T. Pettes, J. Maassen, I. Jo, M. S. Lundstrom and L. Shi, *Nano Lett.*, 2013, **13**, 5316–5322.
- 14 P. Puneet, R. Podila, M. Karakaya, S. Zhu, J. He, T. M. Tritt, M. S. Dresselhaus and A. M. Rao, *Sci. Rep.*, 2013, **3**, DOI: 10.1038/srep03212.
- 15 X. Zhang, J. Wang and S.-C. Zhang, *Phys. Rev. B: Condens. Matter Mater. Phys.*, 2010, **82**, 245107.
- 16 H. Chen, W. Zhu, D. Xiao and Z. Zhang, *Phys. Rev. Lett.*, 2011, **107**, 056804.
- 17 D. S. Kong, W. H. Dang, J. J. Cha, H. Li, S. Meister, H. L. Peng, Z. F. Liu and Y. Cui, *Nano Lett.*, 2010, **10**, 2245–2250.
- 18 D. Teweldebrhan, V. Goyal and A. A. Balandin, *Nano Lett.*, 2010, **10**, 1209–1218.
- 19 Y. Feutelais, B. Legendre, N. Rodier and V. Agafonov, *Mater. Res. Bull.*, 1993, **28**, 591–596.
- 20 W. Richter and C. R. Becker, *Phys. Status Solidi B*, 1977, **84**, 619–628.
- 21 H. Li, J. Cao, W. Zheng, Y. Chen, D. Wu, W. Dang, K. Wang, H. Peng and Z. Liu, *J. Am. Chem. Soc.*, 2012, **134**, 6132–6135.
- 22 H. Peng, W. Dang, J. Cao, Y. Chen, D. Wu, W. Zheng, H. Li, Z.-X. Shen and Z. Liu, *Nat. Chem.*, 2012, **4**, 281–286.
- 23 H. Li, J. Zhang, X. Zhou, G. Lu, Z. Yin, G. Li, T. Wu, F. Boey, S. S. Venkatraman and H. Zhang, *Langmuir*, 2009, **26**, 5603–5609.
- 24 L. Libioulle, A. Bietsch, H. Schmid, B. Michel and E. Delamarche, *Langmuir*, 1998, **15**, 300–304.
- 25 D. Qin, Y. Xia and G. M. Whitesides, *Nat. Protoc.*, 2010, **5**, 491–502.
- 26 S. S. Hong, J. J. Cha, D. Kong and Y. Cui, *Nat. Commun.*, 2012, **3**, 757.
- 27 D. Kim, S. Cho, N. P. Butch, P. Syers, K. Kirshenbaum, S. Adam, J. Paglione and M. S. Fuhrer, *Nat. Phys.*, 2012, **8**, 459–463.
- 28 G. Q. Zhang, W. Wang, X. L. Lu and X. G. Li, *Cryst. Growth Des.*, 2009, **9**, 145–150.
- 29 W. Lu, Y. Ding, Y. Chen, Z. L. Wang and J. Fang, *J. Am. Chem. Soc.*, 2005, **127**, 10112–10116.
- 30 W. Wang, B. Poudel, J. Yang, D. Z. Wang and Z. F. Ren, *J. Am. Chem. Soc.*, 2005, **127**, 13792–13793.
- 31 J. Zhang, Z. P. Peng, A. Soni, Y. Y. Zhao, Y. Xiong, B. Peng, J. B. Wang, M. S. Dresselhaus and Q. H. Xiong, *Nano Lett.*, 2011, **11**, 2407–2414.
- 32 H. Fang, T. Feng, H. Yang, X. Ruan and Y. Wu, *Nano Lett.*, 2013, **13**, 2058–2063.
- 33 M. Zhu, M. Z. Lerum and W. Chen, *Langmuir*, 2011, **28**, 416–423.
- 34 E. T. Vandenberg, L. Bertilsson, B. Liedberg, K. Uvdal, R. Erlandsson, H. Elwing and I. Lundström, *J. Colloid Interface Sci.*, 1991, **147**, 103–118.
- 35 J. Zheng, Z. Zhu, H. Chen and Z. Liu, *Langmuir*, 2000, **16**, 4409–4412.
- 36 R. M. Pasternack, S. Rivillon Amy and Y. J. Chabal, *Langmuir*, 2008, **24**, 12963–12971.
- 37 G. Hao, X. Qi, L. Yang, Y. Liu, J. Li, L. Ren, F. Sun and J. Zhong, *AIP Adv.*, 2012, **2**, 012114–012118.
- 38 J. Israelachvili, *Intermolecular and Surface Forces*, Academic Press, London, 3rd edn, 2011.

